ADVANCED MATERIALS INTERFACES
www.advmatinterfaces.de

The Role of Al_2O_3 ALD Coating on Sn-Based Intermetallic Anodes for Rate Capability and Long-Term Cycling in Lithium-Ion Batteries

Niloofar Soltani, Syed Muhammad Abbas, Martin Hantusch, Sebastian Lehmann, Kornelius Nielsch, Amin Bahrami, and Daria Mikhailova**

The electrochemical performances of $CoSn_2$ and Ni_3Sn_4 as potential anode materials in lithium-ion batteries (LIBs) are investigated using varying thicknesses of an alumina layer deposited by the atomic layer deposition (ALD) technique. Rate capability results showed that at high current densities, Al_2O_3-coated $CoSn_2$ and Ni_3Sn_4 electrodes after 10-ALD cycles outperformed uncoated materials. The charge capacities of coated $CoSn_2$ and Ni_3Sn_4 electrodes are 571 and 134 mAh g^{-1}, respectively, at a high current density of 5 A g^{-1}, while the capacities of uncoated electrodes are 363 and 11 mAh g^{-1}. When the current density is reduced to 1 A g^{-1}, however, the cycling performances of Al_2O_3-coated $CoSn_2$ and Ni_3Sn_4 electrodes fade faster after almost 40 cycles than uncoated electrodes. The explanation is found in the composition of the solid-electrolyte interface (SEI), which strongly depends on the current rate. Thus, X-ray photoelectron spectroscopy analysis of SEI layers on coated samples cycles at a low current density of 0.1 Ag^{-1}, revealed organic carbonates as major products, which probably have a low ionic conductivity. In contrast, the SEI of coated materials cycled at 5 Ag^{-1} consists mostly of mixed inorganic/organic fluorine-rich Al-F and C-F species facilitating a higher ionic transport, which improves electrochemical performance.

1. Introduction

A variety of anode materials have been investigated to meet the growing need for high-performance lithium-ion batteries (LIBs).[1,2] Tin (Sn), which has a theoretical capacity of 992 mAh g^{-1}, which is more than two times higher than that of graphite with a theoretical capacity of 372 mAh g^{-1}, has received a lot of attention in recent years among the numerous alternatives.[3–6] However, the huge volume change of 250% during lithiation/de-lithiation as well as the subsequent rapid capacity fading, significantly limit the application of pure Sn as anode material in LIBs.[7]

Numerous efforts have been made to address this problem. Designing nanostructured Sn-based composites, on the other hand, is one of the most promising techniques to solve this issue. Preparation of composites containing Sn and other inactive metals with respect to Li, such as Fe,[8,9] Ni,[10,11] Cu,[12,13] and Co,[8,14] and others, increased the cyclability of pure Sn to some degree.

The main benefit of inactive metals with a high Young's modulus of elasticity is that they can buffer stress and strain during cycling, allowing volume changes to occur more slowly, delaying disintegration and electrical disconnection.[8,10,11] Inactive materials such as Ni and Co with Young's module values of 207[15] and 205 GPa ,[16] respectively, may therefore be a good option for absorbing the considerable stress induced by large volume expansion of Sn during cycling while keeping contact with the current collector. The buffering effect and also the high electrical conductivity of Ni and Co offer reversible charge–discharge characteristics. In fact, the inactive metal induces sufficient external stress on Sn particles, minimizing the formation of intermediate lithiated phases.

N. Soltani, S. M. Abbas, M. Hantusch, D. Mikhailova
Institute for Complex Materials
Leibniz Institute of Solid State and Materials Science
01069 Dresden, Germany
E-mail: d.mikhailova@ifw-dresden.de

The ORCID identification number(s) for the author(s) of this article can be found under https://doi.org/10.1002/admi.202201598.

DOI: 10.1002/admi.202201598

S. M. Abbas
Vehicle Safety Institute
Graz University of Technology
Graz 8010, Austria

S. Lehmann, K. Nielsch, A. Bahrami
Institute for Metallic Materials
Leibniz Institute of Solid State and Materials Science
01069 Dresden, Germany
E-mail: a.bahrami@ifw-dresden.de

K. Nielsch
Institute of Materials Science
Technische Universität Dresden
01062 Dresden, Germany

Nanostructured electrode materials, on the other hand, displayed destabilized coulombic efficiency after a few cycles. Nanostructured materials can aggregate together during lithiation, forming larger nanoparticles, which pulverize upon subsequent cycling.[17] Furthermore, it should be noted that as particle size decreases, the surface area of the material increases, facilitating the decomposition of carbonate-based electrolytes and irreversible formation of an SEI with adverse properties, resulting in a low coulombic efficiency.[4,18]

On the other hand, applying a mechanically stable and ionically conductive artificial surface layer on nanostructured Sn-based materials is proposed to be a promising method to stabilize the SEI layer while maintaining high capacity. Furthermore, the coating can maintain the electrical path and good physical contact between the electrode material and conductive carbon upon volume expansion and contraction.[19–21]

Due to its excellent ability to provide a conformal coating of thin films on the scale of atomic layers while allowing precise control of the as-deposited film thickness,[22,23] atomic layer deposition (ALD) has been widely used for coating both the cathode and anode surfaces in LIBs among the numerous coating technologies available. Since alumina (Al_2O_3) has been proven to improve the electrochemical performance of TiO_2,[24] SnO_2,[21] Cu—Si,[25] MO_3,[26] natural graphite,[27] Fe_3O_4,[28] and Si[29] electrodes in LIBs, in this study Al_2O_3- coating was investigated as a protective strategy against agglomeration and pulverization of the intermetallic electrode.

In this work, $CoSn_2$ and Ni_3Sn_4 intermetallic materials were synthesized by a solid-state reaction and subsequently crushed using a cryomilling process. After that, ALD coating with various thicknesses of the Al_2O_3-layer corresponding to 5, 10, and 20 cycles were applied directly to the electrodes that are composed of intermetallic powder, carbon conductive, and binder (see **Figure 1**). Herein we demonstrate the effectiveness of the Al_2O_3 coating with an appropriate thickness in increasing the rate performance of the electrodes. Despite the improved electrochemical performance of 10-ALD-coated materials at a high current rate (see Table S2, Supporting Information, for comparison), the relatively poor stability of these materials during cycling at a low current rate of 1 Ag^{-1} showed that alumina coating is not a viable solution for suppressing the electrolyte reduction during long-term cycling.

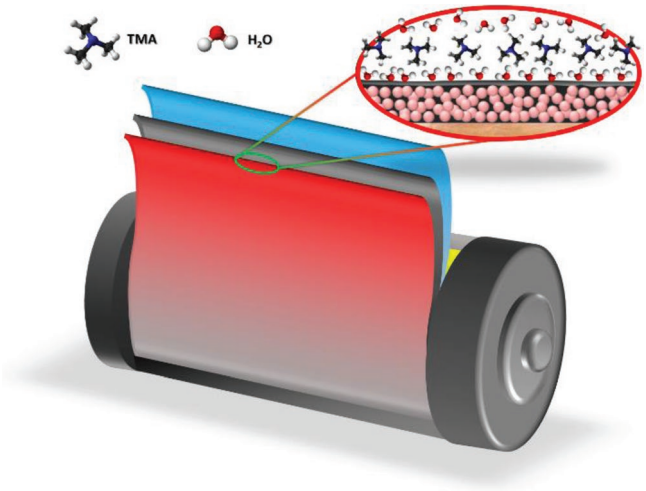

Figure 1. Schematic of protective Al_2O_3 ALD coating on anode layer.

2. Results and Discussions

2.1. Materials Characterization

X-ray diffraction (XRD) was used to evaluate the crystal structure and phase purity of all materials. XRD pattern of the Co—Sn intermetallics with a nominal atomic ratio 1:2 of Co to Sn showed that the powders before milling contain highly crystalline phases of $CoSn_2$ with the space group I4/mcm (ICDD no. 04-001-0930), CoSn with the space group *P6/mmm* (ICDD no.04-004-3134). After the milling process, broad reflections of these two phases were detected, namely of $CoSn_2$ with a crystallite size of 9 nm and weight percentage of 64 wt.%, and CoSn with a crystallite size of 12 nm and weight percentage of 36 wt.% (**Figure 2**a). However, for Ni—Sn intermetallic with a nominal atomic ratio of 3:4 of Ni to Sn, all reflections before and after milling can be indexed as the $Ni_{0.85}Sn$ structure with the space group *C2/m* (ICDD no.04-013-0382). The crystallite size of cryo-milled $Ni_{0.85}Sn$ powders was calculated as 6 nm (Figure 2b).

According to scanning electron microscope (SEM) examination, both cryo-milled Co—Sn and Ni—Sn intermetallic powders have an irregular particle shape and a non-uniform particle size. The determined particle size is in the range of 300 nm to 4 µm (Figures 2c,d).

2.2. Electrochemical Characterization

The effect of alumina coating on cell performance can be better understood by plotting the galvanostatic charge–discharge curves in the differential capacity. The cell polarization properties of uncoated/coated $CoSn_2$ and Ni_3Sn_4 electrodes at 1 A g^{-1} after 20 cycles are depicted as a differential capacity plot in **Figures 3**a,b, respectively. As seen, the potential difference between lithiation and delithiation voltage for both coated samples was minimized by shifting the voltage of lithiation of Li_xSn to a higher voltage, and de-lithiation from the Li_xSn phase to a lower voltage. This means that the SEI layer formed on coated samples allows a more rapid Li-ion diffusion through the ionic conductive film at such a high current density.

The electrochemical performance of coated $CoSn_2$ and Ni_3Sn_4 with 5, 10, and 20 cycles and their uncoated counterparts as electrodes in half cells were evaluated by galvanostatic discharge and charge. To compare the rate capability of the materials, the electrodes were charged and discharged at various current densities between 0.1 and 10 A g^{-1}, and then reversed back to 0.1 A g^{-1} (see **Figures 4**a,c).

As shown in Figure 4a, the rate capability of the 5 and 20-ALD $CoSn_2$ electrodes is inferior to that of the uncoated $CoSn_2$ electrode. It indicates that despite the low thickness of the 5-ALD

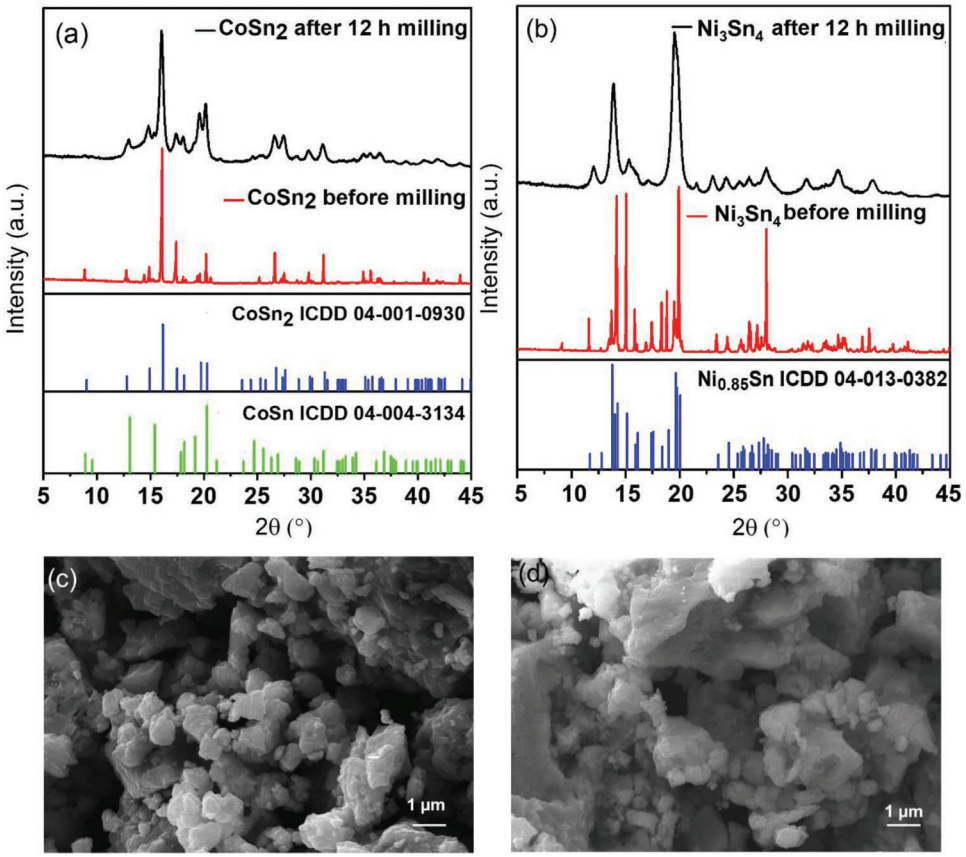

Figure 2. XRD pattern of a) Co-Sn intermetallic before and after cryomilling, respectively, and b) Ni-Sn intermetallic before and after cryomilling, respectively. c,d) SEM image of cryo-milled Co-Sn and Ni-Sn intermetallic, respectively.

sample, it did not improve rate capability, and that the coating layer of the 20-ALD sample is excessively thick, slowing the lithiation kinetics and negatively impacting rate capacity.

However, when compared to the uncoated electrode at the given current densities, the 10-ALD sample showed a better rate capability for all current densities, with lower capacity fade and improved stability at high current densities of 2, 5, and 10 A g^{-1}, with additional capacities of ≈76, 187, and 290 mAh g^{-1}, respectively, over the uncoated electrode. However, it has, like the other samples, rather poor healing properties when it came to the recovering current density to 0.1 A g^{-1}. Despite the fact that the capacity of the 10-ALD sample still retained roughly 600 mAh g^{-1} at 0.1 A g^{-1} after 10 cycles, each cycle resulted in a considerable capacity loss.

Unlike the ALD-$CoSn_2$ samples, however, all 5, 10, and 20-ALD Ni_3Sn_4 electrodes outperformed the uncoated electrode in terms of rate capability. 10-ALD, on the other hand, demonstrated slightly better stability at lower current densities. It shows an additional capacity of 109 and 74 mAh g^{-1} over uncoated electrodes at 2 and 5 A g^{-1}, respectively. Furthermore,

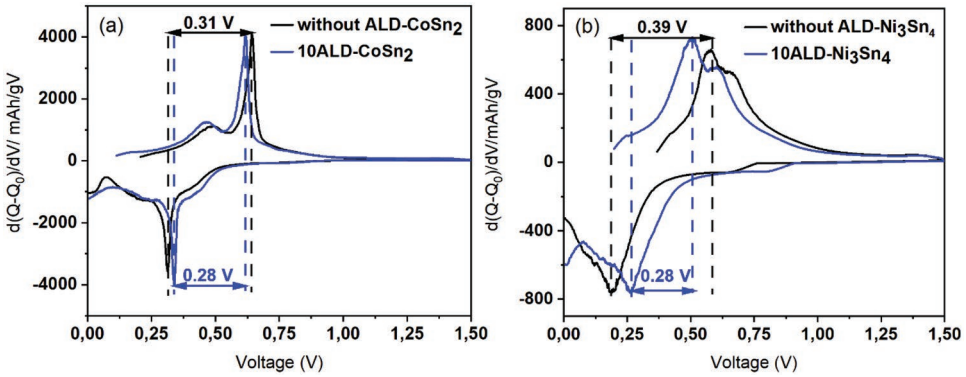

Figure 3. Differential capacity plots at 1 A g^{-1} after 20 cycles a) 10-ALD-$CoSn_2$/uncoated $CoSn_2$ b) 10-ALD-Ni_3Sn_4/uncoated Ni_3Sn_4.

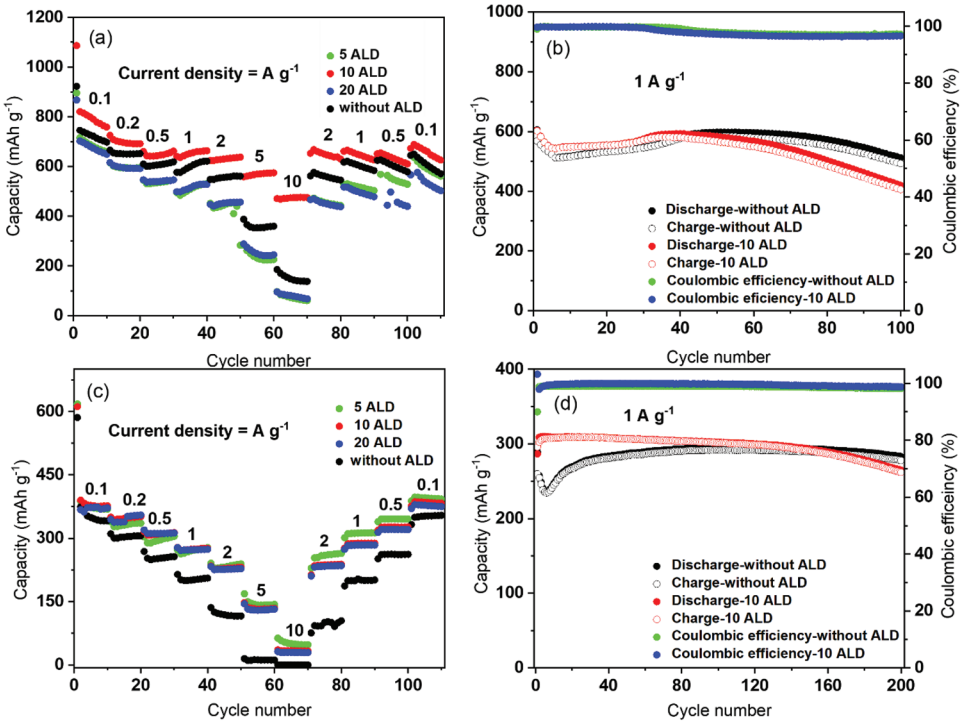

Figure 4. Comparison of rate capability and long-term cycling stability at a current density of 1 A g^{-1} of a,b) coated and uncoated $CoSn_2$ and c,d) coated and uncoated Ni_3Sn_4.

after such high and demanding current densities, ALD-Ni_3Sn_4 electrodes in contrast to ALD-$CoSn_2$ electrodes were able to recover their capacities.

The lower overall capacity of ALD-Ni_3Sn_4 compared to ALD-$CoSn_2$ can be explained by a lower Sn amount in Ni_3Sn_4. This different behavior of Al_2O_3 in these two systems could originate from a different adhesion strength of the coating material to the substrate.[30]

The coulombic efficiencies (CEs) for 10-ALD-$CoSn_2$ and -Ni_3Sn_4, as well as uncoated $CoSn_2$ and Ni_3Sn_4, were calculated at 0.1 Ag^{-1} for the initial charge–discharge cycles, yielding 75.5%, 61.5%, 76.7%, and 62.6%, respectively. The fact that coated samples showed slightly lower CE values than uncoated samples contradicts the hypothesis that Al_2O_3-coating suppresses SEI formation.[24] The higher capacity loss for coated samples during the first charge–discharge cycle implies a higher Li consumption by Al_2O_3-coated materials. XPS studies of the formed SEI (Figures 5,6) on the surface of uncoated and coated electrodes can shed light on the low CE during the first charge–discharge cycle of electrode materials.

To investigate the SEI composition as a function of cell voltage, uncoated $CoSn_2$, Ni_3Sn_4, and coated $CoSn_2$ samples were discharged to 0.6, 0.2, and 0.005 V versus Li/Li^+. As shown in **Figure 5**, for all samples regardless of the voltage, carbon, lithium, oxygen, and fluorine are the majority elements of the SEI layer. As the voltage decreased, the quantities of each element also were changed. The electrode materials have a certain impact on the element concentration of the resulting SEI layer. The surface coating has additionally changed the chemistry of SEI formation during the discharging process, resulting in a variety of SEI compositions.

Since the electrode surface included ≈1 wt.% Sn at 0.6 V and less than 0.04 wt.% Sn at 0.005 V, we can deduce a relatively thick developed SEI.[31,32] However, an analysis of the elemental composition showed that the SEI formed on coated samples at a low current rate of 0.1 Ag^{-1} has much more carbon-containing species than that on uncoated samples. Although alumina coating has no obvious effect on the thickness of the SEI layer, its cracking upon Sn volume expansion provided more susceptible sites for excessive solvent reduction, leading to a porous-structured SEI layer (see **Figure 7**a,b). The almost equal concentration of Li, C, and O in the SEI layer of the uncoated samples suggests a multicomponent, inorganic-rich, and denser SEI layer (see Figure 7c,d).

For further study of compositional change of SEI grown on $CoSn_2$ surfaces, three core peaks of C 1s, O 1s, and F 1s, depicted in **Figure 6**, are comprehensively analyzed. At 284.4, 286.2, 287.7, and 289.5 eV, the C 1s spectrum of the uncoated $CoSn_2$ sample discharged to 0.6 V revealed four peaks. Conductive carbon (C—C) is responsible for the peak at 284.4 eV. However, the conductive carbon signal dropped as the voltage was decreased to 0.2 V, suggesting the formation of a thick SEI layer. The signal at 286.2 eV is attributed to an O—C—O group in CH_3OLi, which has the maximum intensity in the sample discharged at 0.6 V, whereas the peaks at 287.7 and 289.5 eV are attributed to C—F/O—C—O and Li_2CO_3, respectively. The detected O—C—O bond is due to the organic components attached to the electrode surface after the solvent decomposition and the decomposed organic components, such as R—O—Li, are deposited on the surface of uncoated sample.

The presence of a carbonate group peak at 289.5 eV for the sample discharged at 0.6 V was corroborated by the binding

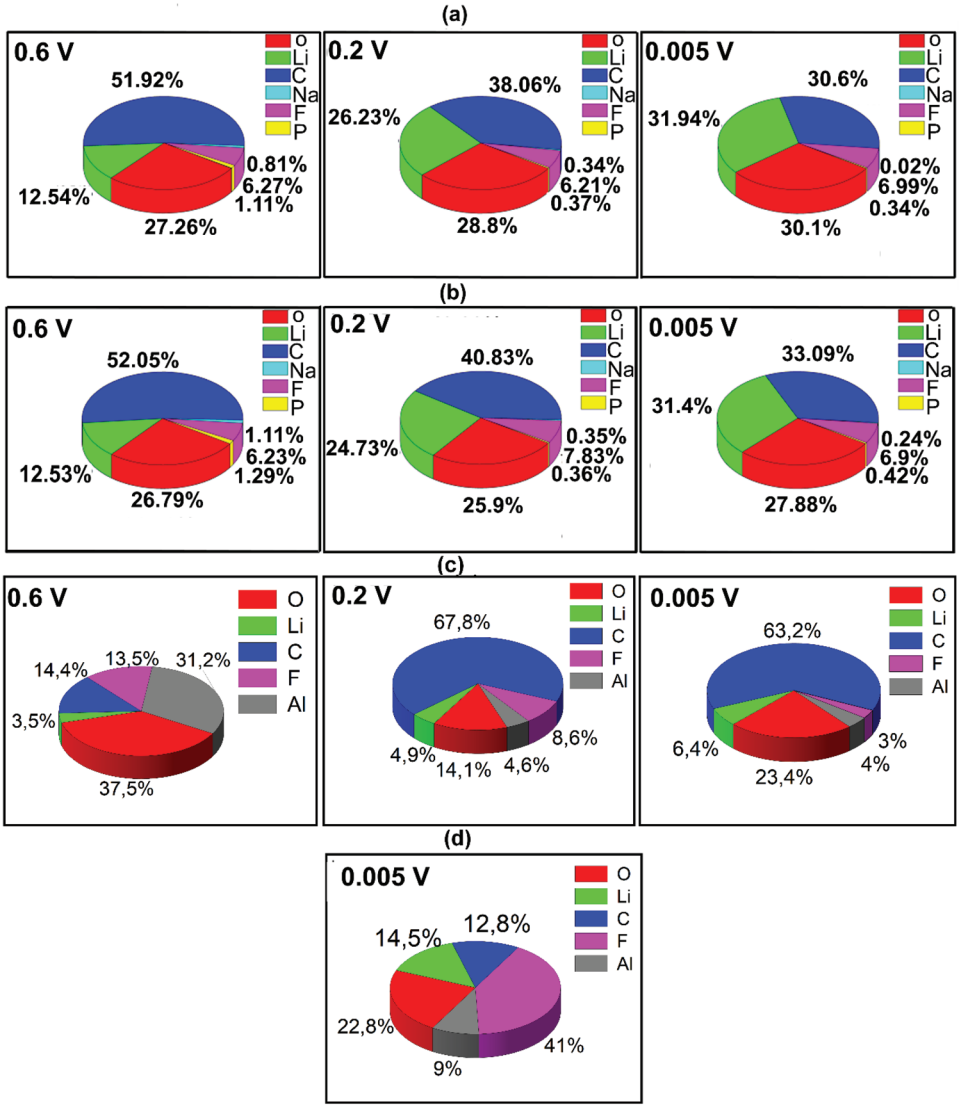

Figure 5. XPS analysis showing concentrations of the elements at the surface of a) Ni_3Sn_4 and b) $CoSn_2$ without coating; c) coated $CoSn_2$ discharged to 0.6, 0.2 and 0.005 V at 0.1 Ag^{-1} and d) coated $CoSn_2$ discharged to 0.005 V at 5 Ag^{-1}.

energy of carbonyl oxygen at 532.8 eV in the O 1s spectrum. However, no trace of carbonyl oxygen was found at lower voltages.[33,34] This peak results from the reaction of released O_2 and electrolyte on the electrode.[35]

A peak at 686 eV in the F 1s spectrum for an uncoated sample discharged at 0.6 V is attributed to LiF, which was formed from the decomposition of FEC at a higher voltage. However, by decreasing the voltage to 0.2 V the intensity of the LiF peak decreased dramatically, and a peak at a binding energy of 687.3 eV, which corresponds to a C−F, was intensified, which is in coincidence with the increase in the intensity of the C 1s peak at 287.7 eV.[33,34]

Besides, another new C 1s feature at ≈290.8 eV at a voltage lower than 0.6 V can be observed. This signal is attributed to the carbonate group (−CHF−OCO_2-type) resulting from further FEC decomposition and $LiPF_6$ degradation. On the other hand, the C 1s spectra of the SEI layer formed on the coated $CoSn_2$ at 0.6 V revealed the presence of a weak peak at ≈283.2 and a strong peak at 285.5 eV associated with carbide-like species like $LiCH_2CH_2OCO_2$ from the reduction of ethylene carbonate (EC), and −C=O species, respectively. The dominating signal remained at 285.5 V when the voltage was reduced to 0.2. The Al 2p spectrum after samples discharge to 0.6 V is mainly composed of species with Al−O bonds at 74.3 eV. By decreasing the voltage to 0.005 V, at the surface of the electrode new Al 2p peaks, corresponding to Al−F (76.6 eV), and Al−Li−O (73.6 eV) bonds, appeared. In the F1s spectrum, LiF and C−F species can be detected at discharge voltages 0.6 and 0.2 V, while only C−F species remained at 0.005 V.[36–38]

The XPS results for the uncoated sample allowed us to conclude that at higher voltage, SEI is mainly composed of inorganic species like LiF and lithium carbonate as well as semi-organic compounds such as CH_3OLi.[33,34] However, the

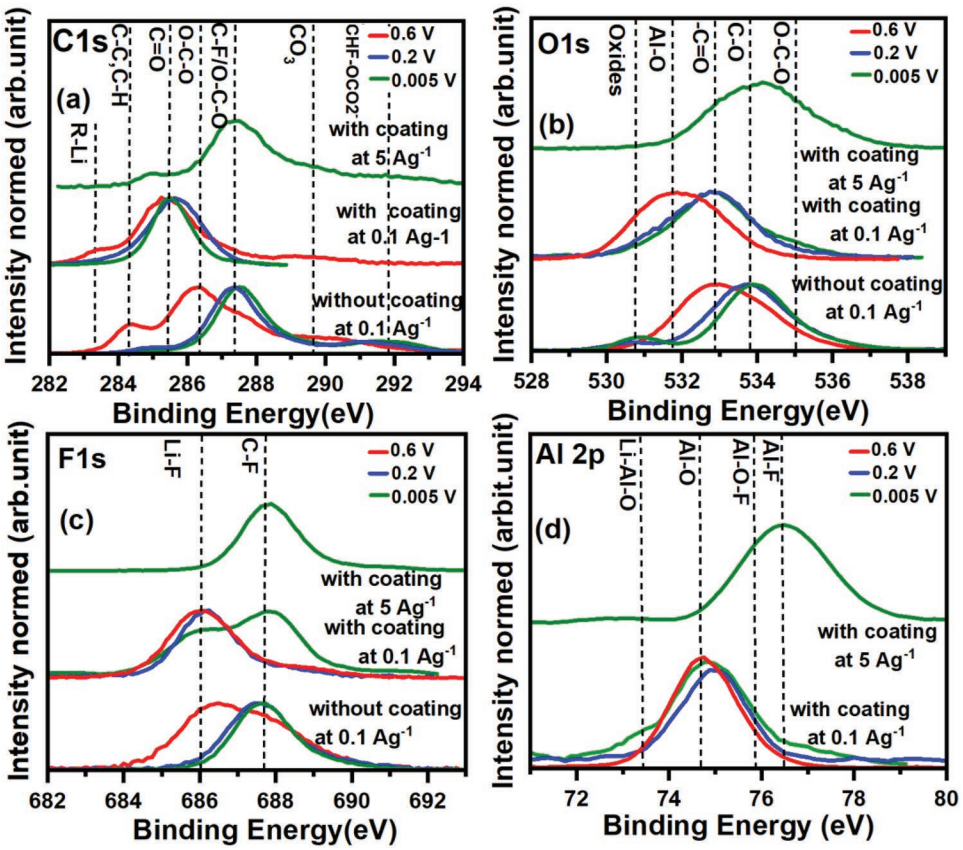

Figure 6. High resolution of a) C1s, b) O 1s, c) F 1s, and d) Al 2p spectra of uncoated and 10-ALD coated $CoSn_2$ electrode discharged to 0.6, 0.2, and 0.005 V at 0.1 A g^{-1} and 5 A g^{-1}.

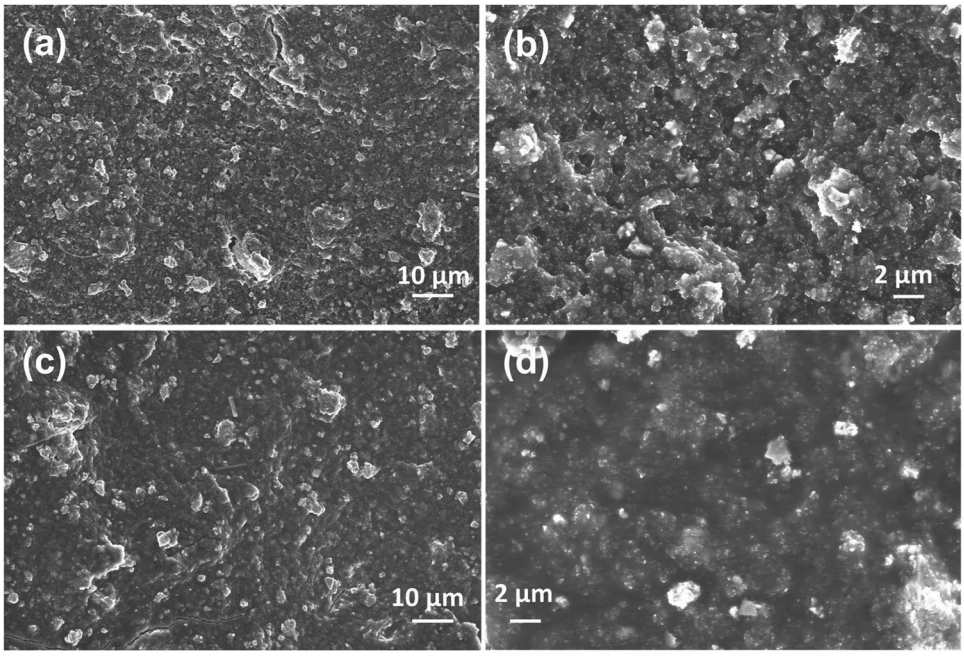

Figure 7. SEM image showing the morphology of the SEI layer formed on electrode at 0.1 A g^{-1} after 20 cycles; a,b) 10-ALD coated $CoSn_2$ electrode and c,d) $CoSn_2$ electrode without coating.

upper layer of SEI at the lower voltage of 0.2 V is composed of inorganic products of lithium-fluorinated carbon salts.

In contrast to the SEI layer of coated $CoSn_2$ at a higher voltage, which is mostly made up of Al—O species corresponding to the originally existing Al_2O_3 artificial SEI layer, when the voltage decreased, the increasing amount of CO_x organic species indicates a substantial solvent reduction. It demonstrates that the alumina coating is prone to rupture due to the volume change of the electrode materials, providing sites for additional electrolyte reduction, which can adversely affect the capacity in subsequent cycles. Li^+ transport is therefore gradually decreased as the result of porous organic compounds formation with low Young's modulus, low ionic conductivity, and low physicochemical stability, causing capacity fade over cycles.[39]

However, as seen in Figure 6d the formation of porous organic components with low ionic conductivity in the SEI layer is significantly suspended at a high current rate of 5 Ag^{-1}, whereas the formation of uniform Al-F species as a protective and ionically conductive layer allows charge transfer, validating a high rate performance of coated samples. The crack formation in alumina at higher current rates is smaller than that at lower current densities, since the diffusivity of Li in bulk Sn—Co samples is reduced, thus leading to less-pronounced lithiation of Sn and a less volume expansion. Therefore, the Al_2O_3-protection of the electrode surface against reaction with the electrolyte is higher. This can also infer indirectly from a smaller carbon content in the $CoSn_2$ surface that comes from the severe reduction of the electrolyte.

The cycling performances of 10-ALD-$CoSn_2$ and Ni_3Sn_4 samples using conventional carbonate electrolyte (LP30) showed high charge capacities of 580 and 308 mAh g^{-1} after 40 cycles at 1 A g^{-1}, respectively (see Figure 4b,d). However, after 40 cycles the charge capacity of coated electrodes faded faster compared to that for uncoated electrodes that may be attributed to the rupture of alumina during cycling.[40] Indeed, the propagation of a crack in alumina film during the volume change of the underlying Sn-based alloys during cycling destroyed the integrity of alumina and electrode materials leading to considerable porous organic SEI formation and loss in electronic conductivity. This observation is in good agreement with the results of the EIS measurements (see Figure S4, Supporting Information). It revealed that R_{ct} values for coated and uncoated samples cycled at 1 A g^{-1} after 100 cycles were remarkably similar, indicating that the coating may not be sufficiently insulating and durable to serve as a suitable preformed SEI.

Figure S5a–c (Supporting Information) also depicts the voltage profile for coated and uncoated $CoSn_2$ at 10 A g^{-1} and long-term cycling stability of coated $CoSn_2$ for 100 cycles at current densities of 2 and 10 A g^{-1}. The results showed that despite the high capacity of 10-ALD-$CoSn_2$ that is superior in comparison to the majority of investigated Co—Sn materials, particularly at 10 Ag^{-1}, coated electrodes started to fade capacity after ≈40 cycles. Although the crack formation in alumina at higher current rates is smaller than that at lower current densities, however, at such a high current rate for higher cycles, the increased stress on the electrodes from rapid volume change, the alumina cannot buffer the volumetric change of $CoSn_2$ and prevent them from collapsing. The huge volume change mismatch during charging and discharging at the interface between the coating and $CoSn_2$ results in a poor interface bonding between these two phases that makes the coatings easily detach during cycling. This repetitive volume change can aggravate the alumina layer fracture and induce a rapid reduction of the electrolyte until the electrolyte is completely consumed.

Figure S6 (Supporting Information) illustrates the long-term cycling stability of 10-ALD-coated $CoSn_2$ and Ni_3Sn_4 using LiTFSI/DOL+DME electrolytes at a current density of 1 A g^{-1}. Both samples exhibit severe irreversibility during the first 40 cycles. Further cycling reduces the capacity of coated Ni_3Sn_4 and $CoSn_2$ from 369 and 349 mAh g^{-1} at the 40th cycle to 187 and 310 mAh g^{-1} at the 100th cycle, respectively, which is less than the capacity gain in LP30. These findings show that switching from the traditional carbonate electrolyte (LP30) to LiTFSI/DOL+DME does not improve at all the cyclability of coated samples.

3. Conclusion

In summary, Al_2O_3 layers with the various thickness (5, 10, and 20 cycles) were deposited on $CoSn_2$ and Ni_3Sn_4 electrode layers using the ALD technique. It was demonstrated that the Al_2O_3-coating with 10 cycles has a positive effect on the rate capability of $CoSn_2$ and Ni_3Sn_4 electrodes, which is essential for practical applications in batteries. Another crucial factor for practical application is the capacity retention of coated $CoSn_2$ in long-cycle performance. Although the coated $CoSn_2$ has some capacity fading after longer cycling, still it has a capacity of 223 mAh g^{-1} after 120 cycles without any noticeable changes in cell polarization and outperforms the uncoated samples. XPS studies demonstrated that SEI formed on alumina-coated samples is predominantly composed of organic carbonates at 0.1 Ag^{-1}, in contrast to the formation of a nonporous multicomponent inorganic-rich SEI layer for uncoated samples. The high carbon content of the SEI layer reflects the severe reduction of EC molecules, which can be caused and promoted by arising alumina cracks during cycling. This resulted in carbonate-rich components of the SEI layer, which may help to explain why the capacity of coated samples starts to fade in the subsequent cycles. Based on XPS results showing current-rate dependent SEI formation, it was revealed that at a high current density of 5 Ag^{-1}, the growth of organic components with low ionic conductivity in the SEI layer was significantly diminished while the formation of mixed inorganic/organic components of Al—F and C—F was favored enabling a faster transport of lithium through the SEI. Nevertheless, after longer cycling, despite the high capacity of 10-ALD-$CoSn_2$, particularly at high current rate, it began to fade capacity. These finding show independent of current density during charge–discharge cycling, the SEI layer will break more when it comes to active electrode materials like Sn and Si that experience significant volume changes during lithiation–delithiation. Indeed, the crystalline structure of Sn leads crack formation along the certain orientations. Consequently, in order to increase the efficiency of alumina, we must consider the materials with a lower volume change

as well as materials with a more amorphous structure and isotropic volumetric expansion.

4. Experimental Section

Synthesis of Ni_3Sn_4 and $CoSn_2$ Particles: Ingots with a nominal composition of Ni_3Sn_4 and $CoSn_2$ were prepared by a solid-state reaction method. High purity elements Sn (99.99%), Ni (99.99%), and Co (99.99%) with suitable proportions were put into a quartz tube. The evacuated quartz tube was then placed into an oven and heated up gradually with a slow heating rate that was close to equilibrium conditions (see Figure S1, Supporting Information). To complete the reaction and facilitate the homogenization process, the obtained ingots were then ball-milled for ≈12 h at liquid nitrogen temperature (77 K) by a cryogenic ball miller (Retsch Cryomill). The ball to material-weight ratio was 25:1.

Synthesis of ALD-Al_2O_3 Coated Ni_3Sn_4 and $CoSn_2$ Electrodes: For the preparation of the working electrode, a slurry of intermetallic powders as an active material, carbon black (C-NERGY Super C65 from TIMCAL Belgium) as a conductive additive, and sodium carboxymethyl cellulose (CMC, Aqualon 7L) as a binder in 64: 21: 15 weight ratios were homogenized in a Retsch MM200 mixer mill at 20 Hz for 30 min. The prepared slurry was blade-coated onto 9 µm thin copper foil (MTI). After drying in air at 80 °C for 2 h, 11 mm electrode discs with a mass loading of ≈1 mg cm^{-2} were punched and assembled in cells. 250 µL of 1 M solution of $LiPF_6$ in a mixture of ethylene carbonate/dimethyl carbonate in a volume ratio of 1:1 were used as an electrolyte (LP30, BASF). To improve cycling stability, 10 µL fluoroethylene carbonate (99% FEC, Sigma-Aldrich) was added to the electrolyte. Lithium bis(trifluoromethylsulphonyl)imide (LiTFSI, BASF) in 1,3-dioxolane (DOL, BASF) /1,2- dimethoxyethane (DME, BASF) (1:1, v/v) was also employed as an electrolyte to investigate the effect of the electrolyte composition on the long-term cyclability of intermetallic electrodes. The cells were assembled with two layers of Whatman glass fiber as a separator in an Ar-filled glovebox with H_2O and O_2 contents <0.1 ppm.

The effect of thickness of Al_2O_3-ALD coating on the electrochemical performances of electrodes has been studied. Al_2O_3 films were deposited by ALD in a Veeco Savannah S200 reactor. Trimethylaluminium ($Al(CH_3)_3$) and water (H_2O) were used as reactants. The chamber temperature was set to 150 °C during deposition. The thickness of deposited Al_2O_3-layers was estimated from the growth speed per cycle value corresponding to ≈1.4 Å $cycle^{-1}$. Thus, ALD processes of 5, 10, and 20 cycles led to nominal Al_2O_3 coating thicknesses of 0.7, 1.4, and 2.8 nm, respectively.

Electrochemical Measurements: Electrochemical studies on Al_2O_3-coated materials as well as uncoated materials as references were performed using a VMP3 (Biologic, France) multichannel potentiostatic–galvanostatic system in standard two-electrode Swagelok-type cells with metallic Li chips (12 mm diameter, 250 µm thickness, g-materials) as a counter and a reference electrode. Galvanostatic charge-discharge measurements with a potential limitation (GCPL) were conducted in a potential window between 0.005 and 1.50 V versus Li/Li^+, at various current densities of 0.1, 0.2, 0.5, 1, 2, 5, 10 A g^{-1}. The specific capacity and current densities were calculated based on the mass of intermetallic materials in the electrode. Potentiostatic impedance spectroscopy (PEIS) measurements were performed with $\Delta V = 5$ mV between 0.01 Hz and 100 kHz, and every frequency was measured five times.

Characterizations: The intermetallic powders were chemically analyzed by inductively coupled plasma-optical emission spectrometry ICP-OES (SPECTRO ARCOS II MVThermo Fisher Scientific iCAP 6500 Dual View). For this, the samples were dissolved in 5 mL HNO_3 (65%) and 1 mL HF (35%) (Table S1, Supporting Information). XRD measurements of intermetallics were performed on a STOE STADI P diffractometer with Mo $K_{\alpha 1}$ radiation with a step size of $\Delta_{2\theta} = 0.5°$ and an exposure time of 250 s per step. To increase the intensity of reflections, powders obtained after the cryomilling process were measured with a step size of $\Delta_{2\theta} = 0.5°$ and an exposure time of 650 s per step. The crystallite size of the obtained particles was calculated by Scherrer's equation

$$L = \frac{K\lambda}{H \times \cos\theta} \quad (1)$$

where L is an average crystallite size, λ is the wavelength of Mo $K_{\alpha 1}$, K is the shape parameter that is 0.94 for spherical shape, H is the full width at a half maximum (in radian), and θ is the corresponding Bragg angle (°).

The SEM images of the powders were taken with a LEO GEMINI 1530 at 20 kV acceleration voltage using the secondary electron detector.

To study the SEI layer composition formed on intermetallic electrodes, half cells discharged to a given voltage of 0.6, 0.2, 0.005 V at a current density of 0.1 and 5 A g^{-1} were disassembled in the lithiated state inside a glove box. Each electrode was washed three times in 1 mL DMC to remove the residual electrolyte with minimal damage to the SEI layer, and dried in a vacuum. Finally, they were mounted in a sealed XPS holder to avoid air exposure. XPS was carried out using a Physical Electronics PHI 5600 CI system. An Al K_α X-ray source (350 W) was used at pass energy of 29 eV. Since the O 1s spectrum recorded at the Al K_α X-ray source overlaps with the Na 1s spectrum, a 400 W Mg K_α X-ray source at a pass energy of 29 eV was applied to obtain a high-resolution O 1s spectrum. The binding energy scale was calibrated with a C 1s peak maximum at 284.8 eV for sp^2 carbon. The deposition of Al_2O_3-ALD on electrodes has been confirmed with help of XPS and EDX techniques (Figures S2 and S3, Supporting Information).

Supporting Information

Supporting Information is available from the Wiley Online Library or from the author.

Acknowledgements

N.S. and A.B. acknowledges the Alexander von Humboldt Foundation for the Postdoctoral Research Fellow funding.

Open access funding enabled and organized by Projekt DEAL.

Conflict of Interest

The authors declare no conflict of interest.

Data Availability Statement

The data that support the findings of this study are available on request from the corresponding author. The data are not publicly available due to privacy or ethical restrictions.

Keywords

anode materials, atomic layer deposition, $CoSn_2$, Li-ion batteries, Ni_3Sn_4

Received: July 20, 2022
Revised: September 16, 2022
Published online: October 3, 2022

[1] S. Goriparti, E. Miele, F. De Angelis, E. Di Fabrizio, R. Proietti Zaccaria, C. Capiglia, *J. Power Sources* **2014**, *257*, 421.

[2] M. V. Reddy, G. V. Subba Rao, B. V. R. Chowdari, *Chem. Rev.* **2013**, *113*, 5364.

[3] S. Liang, Y.-J. Cheng, J. Zhu, Y. Xia, P. Müller-Buschbaum, *Small Methods* **2020**, *4*, 2000218.
[4] F. Xin, M. S. Whittingham, *Electrochem. Energy Rev.* **2020**, *3*, 643.
[5] N. Soltani, A. D. C. Permana, S. Donath, D. Mikhailova, *Mater. Today Commun.* **2021**, *29*, 102965.
[6] N. Soltani, A. Bahrami, L. Giebeler, T. Gemming, D. Mikhailova, *Prog. Energy Combust. Sci.* **2021**, *87*, 100929.
[7] M. Winter, J. O. Besenhard, *Electrochim. Acta* **1999**, *45*, 31.
[8] S. Wang, M. He, M. Walter, F. Krumeich, K. V. Kravchyk, M. V. Kovalenko, *Nanoscale* **2018**, *10*, 6827.
[9] F. Xin, H. Zhou, Q. Yin, Y. Shi, F. Omenya, G. Zhou, M. S. Whittingham, *ACS Omega* **2019**, *4*, 4888.
[10] J. Liu, Y. Wen, P. A. van Aken, J. Maier, Y. Yu, *Nano Lett.* **2014**, *14*, 6387.
[11] J. Hassoun, S. Panero, B. Scrosati, *J. Power Sources* **2006**, *160*, 1336.
[12] S. D. Beattie, J. R. Dahn, *J. Electrochem. Soc.* **2003**, *150*, A894.
[13] Y. N. Wang, J. Y. Jiang, X. X. Liu, X. Liu, Y. Xiang, R. Wu, Y. Chen, J. S. Chen, *Electrochim. Acta* **2020**, *336*, 135690.
[14] X. Shi, H. Song, A. Li, X. Chen, J. Zhou, Z. Ma, *J. Mater. Chem. A* **2017**, *5*, 5873.
[15] A. V. Shatov, S. Ponomarev, S. Firstov, *Comprehensive hard materials*, Elsevier, MA, USA **2014**, pp. 267–299.
[16] J. K. Luo, A. J. Flewitt, S. M. Spearing, N. A. Fleck, W. I. Milne, *Mater. Lett.* **2004**, *58*, 2306.
[17] J. Wang, F. Fan, Y. Liu, K. L. Jungjohann, S. W. Lee, S. X. Mao, X. Liu, T. Zhu, *J. Electrochem. Soc.* **2014**, *161*, F3019.
[18] J.-S. Bridel, S. Grugeon, S. Laruelle, J. Hassoun, P. Reale, B. Scrosati, J.-M. Tarascon, *J. Power Sources* **2010**, *195*, 2036.
[19] J. Liu, X. Meng, M. N. Banis, M. Cai, R. Li, X. Sun, *J. Phys. Chem. C* **2012**, *116*, 14656.
[20] S. Lu, H. Wang, J. Zhou, X. Wu, W. Qin, *Nanoscale* **2017**, *9*, 1184.
[21] D. Wang, J. Yang, J. Liu, X. Li, R. Li, M. Cai, T.-K. Sham, X. Sun, *J. Mater. Chem. A* **2014**, *2*, 2306.
[22] S. He, A. Bahrami, X. Zhang, I. G. Martínez, S. Lehmann, K. Nielsch, *Adv. Mater. Technol.* **2022**, *7*, 2100953.
[23] J. Yang, A. Bahrami, X. Ding, P. Zhao, S. He, S. Lehmann, M. Laitinen, J. Julin, M. Kivekäs, T. Sajavaara, K. Nielsch, *Adv. Electron. Mater.* **2022**, *8*, 2101334.
[24] H. Sopha, G. D. Salian, R. Zazpe, J. Prikryl, L. Hromadko, T. Djenizian, J. M. Macak, *ACS Omega* **2017**, *2*, 2749.
[25] F.-F. Cao, J.-W. Deng, S. Xin, H.-X. Ji, O. G. Schmidt, L.-J. Wan, Y.-G. Guo, *Adv. Mater.* **2011**, *23*, 4415.
[26] L. A. Riley, A. S. Cavanagh, S. M. George, Y. S. Jung, Y. Yan, S.-H. Lee, A. C. Dillon, *ChemPhysChem* **2010**, *11*, 2124.
[27] Y. S. Jung, A. S. Cavanagh, L. A. Riley, S.-H. Kang, A. C. Dillon, M. D. Groner, S. M. George, S.-H. Lee, *Adv. Mater.* **2010**, *22*, 2172.
[28] Q.-H. Wu, B. Qu, J. Tang, C. Wang, D. Wang, Y. Li, J.-G. Ren, *Electrochim. Acta* **2015**, *156*, 147.
[29] S. Hy, Y.-H. Chen, H.-M. Cheng, C.-J. Pan, J.-H. Cheng, J. Rick, B.-J. Hwang, *ACS Appl. Mater. Interfaces* **2015**, *7*, 13801.
[30] D. Naumenko, B. A. Pint, W. J. Quadakkers, *Oxid. Met.* **2016**, *86*, 1.
[31] J.-T. Li, J. Świątowska, V. Maurice, A. Seyeux, L. Huang, S.-G. Sun, P. Marcus, *J. Phys. Chem. C* **2011**, *115*, 7012.
[32] J.-T. Li, J. Swiatowska, A. Seyeux, L. Huang, V. Maurice, S.-G. Sun, P. Marcus, *J. Power Sources* **2010**, *195*, 8251.
[33] C. Xu, F. Lindgren, B. Philippe, M. Gorgoi, F. Björefors, K. Edström, T. Gustafsson, *Chem. Mater.* **2015**, *27*, 2591.
[34] T. Jaumann, J. Balach, M. Klose, S. Oswald, U. Langklotz, A. Michaelis, J. Eckert, L. Giebeler, *Phys. Chem. Chem. Phys.* **2015**, *17*, 24956.
[35] H. Yu, X. He, X. Liang, *ACS Appl. Mater. Interfaces* **2022**, *14*, 3991.
[36] S. Verdier, L. El Ouatani, R. Dedryvère, F. Bonhomme, P. Biensan, D. Gonbeau, *J. Electrochem. Soc.* **2007**, *154*, A1088.
[37] Z. W. Lebens-Higgins, D. M. Halat, N. V. Faenza, M. J. Wahila, M. Mascheck, T. Wiell, S. K. Eriksson, P. Palmgren, J. Rodriguez, F. Badway, N. Pereira, G. G. Amatucci, T.-L. Lee, C. P. Grey, L. F. J. Piper, *Sci. Rep.* **2019**, *9*, 17720.
[38] K. Kanamura, T. Umegaki, S. Shiraishi, M. Ohashi, Z.-i. Takehara, *J. Electrochem. Soc.* **2002**, *149*, A185.
[39] Y. Xu, K. Dong, Y. Jie, P. Adelhelm, Y. Chen, L. Xu, P. Yu, J. Kim, Z. Kochovski, Z. Yu, W. Li, J. LeBeau, Y. Shao-Horn, R. Cao, S. Jiao, T. Cheng, I. Manke, Y. Lu, *Adv. Energy Mater.* **2022**, *12*, 2200398.
[40] L. A. Riley, A. S. Cavanagh, S. M. George, Y. S. Jung, Y. Yan, S.-H. Lee, A. C. Dillon, *ChemPhysChem* **2010**, *11*, 2124.